

A survey for the missing hydrogen in high redshift radio sources

S. J. Curran^{1,2*}, M. T. Whiting³, E. M. Sadler^{1,2} and C. Bignell⁴

¹*Sydney Institute for Astronomy, School of Physics, The University of Sydney, NSW 2006, Australia*

²*ARC Centre of Excellence for All-sky Astrophysics (CAASTRO)*

³*CSIRO Astronomy and Space Science, PO Box 76, Epping NSW 1710, Australia*

⁴*National Radio Astronomy Observatory, P.O. Box 2, Rt. 28/92 Green Bank, WV 24944-0002, USA*

Accepted —. Received —; in original form —

ABSTRACT

Unlike at lower redshift, where there is a 40% detection rate, surveys for 21-cm absorption arising within the hosts of $z \gtrsim 1$ radio galaxies and quasars have been remarkably unsuccessful. Curran et al. (2008) suggest that this is due to the high redshift selection biasing towards the most optically bright objects (those most luminous in the ultra-violet in the rest-frame), where the gas is ionised by the active galactic nucleus. They therefore argue that there must be a population of fainter objects in which the hydrogen is not ionised and which exhibit a similar detection rate as at lower redshifts. In order to find this “missing” gas at high redshift, we have therefore undertaken a survey of $z \gtrsim 2$ radio sources, selected by optical faintness. Despite having optical magnitudes which indicate that the targets have ultra-violet luminosities below the threshold where all of the gas is ionised, there were no detections in any of the eight sources for which useable data were obtained. Upon an analysis of the spectral energy distributions, ionising photon rates can only be determined for three of these, all of which suggest that the objects are *above* the highest luminosity of a current 21-cm detection. The possibility that the other five could be located at lower photon rates cannot be ruled out, although zero detections out of five is not statistically significant. Another possible cause of the non-detections is that our selection biases the sample towards sources which are very steep in the radio band, with a mean spectral index of $\langle \alpha \rangle = -1.0$, cf. -0.3 for both the 21-cm detections and UV luminous non-detections. This adds the further possibility that the sources have very extended emission, which would have the effect of reducing the coverage by the putative absorbing gas, thus decreasing the sensitivity of the observation.

Key words: galaxies: active – quasars: absorption lines – radio lines: galaxies – ultra violet: galaxies – galaxies: stellar content – galaxies: high redshift

1 INTRODUCTION AND SAMPLE SELECTION

Redshifted H I 21-cm provides a probe of the most abundant element in the Universe, through surveys which are not subject to the flux limitations of optical surveys. In absorption, 21-cm probes the cool component of the neutral gas, which is the reservoir of raw material ultimately responsible for all star formation. Furthermore, the strength of the absorption depends only upon the column density of the absorber and the flux of the background source, making the 21-cm transition potentially detectable up to redshifts of $z \sim 50$, where the ionosphere begins to affect the $\lesssim 30$ MHz radio waves.

Despite this, redshifted 21-cm absorption is currently rare, with only 78 absorbers known at $z \geq 0.1$, 80% of which are detected at $z \lesssim 1$. Much of this is due to the past availability of interference free bands at low frequencies, although there are additional selection effects at play:

- For absorbers *intervening* the sight-lines to more distant radio sources, the 60% detection rate at $z \leq 1$, compared to 20% at $z \geq 1$, in systems known to have high hydrogen column densities¹, can be attributed to the geometry effects introduced by an expanding Universe, where the coverage of the background flux is systematically lower at redshifts of $z \gtrsim 1$ (Curran & Webb 2006; Curran 2012).

- For absorbers *associated* with the radio source itself, the detection rate at $z \lesssim 1$ is 40%, compared to 17% at $z \gtrsim 1$ (Curran & Whiting 2010). This is believed to be due to the higher redshifts biasing towards the most ultra-violet luminous objects, where the intense flux ionises the gas. Specifically, associated 21-cm absorption has *never* been detected where the $\lambda = 1216$ Å continuum luminosity of the active galactic nucleus (AGN) exceeds $L_{1216} \sim 10^{23} \text{ W Hz}^{-1}$ (Curran et al. 2008 and recently confirmed

* E-mail: sjc@physics.usyd.edu.au

¹ Damped Lyman- α absorption systems (DLAs), with neutral hydrogen column densities of $N_{\text{HI}} \geq 2 \times 10^{20} \text{ cm}^{-2}$.

by Grasha & Darling 2011). At these frequencies (2.47×10^{15} Hz) and above, the photons have enough energy to excite the hydrogen beyond the ground state, so that it cannot absorb in 21-cm. Curran & Whiting (2012) have extended this to the ionising ($\lambda \leq 912 \text{ \AA}$) radiation and show that a similar (i.e. $L_{912} \sim 10^{23} \text{ W Hz}^{-1}$) cut-off also applies. The large fraction of non-detections at high redshift are therefore due to the flux limited nature of the optical surveys selecting the brightest objects, where the observed-frame optical light is rest-frame ultra-violet, in which all of the gas is believed to be ionised (Curran & Whiting 2012).

In order to find the neutral gas missing from high redshift AGN, we suggest that high redshift 21-cm surveys should be directed towards the most optically faint sources. We have therefore embarked on an observing campaign of objects selected by faint optical magnitudes. As discussed in Curran et al. (2011d), our usual source catalogue, the Parkes Half-Jansky Flat-spectrum Sample (PHFS, Drinkwater et al. 1997), yielded only two sources with faint blue magnitudes ($B \gtrsim 22$) in the 90-cm band ($z = 3.09 - 3.63$)², both of which have been previously searched for in 21-cm (Curran et al. 2008). We therefore compiled all available radio catalogues, which give both redshifts and magnitudes, and selected those with B, V, R or I magnitudes which indicate that $L_{1216} \lesssim 10^{23} \text{ W Hz}^{-1}$ at the given redshift (Fig. 1). We further shortlisted those in which 21-cm is redshifted into the 290–395 MHz band of the Green Bank Telescope (GBT) or the UHF-low band (250–460 MHz) of the Westerbork Synthesis Radio Telescope (WSRT) and which reached sufficiently high elevations at these locations, while having flux densities estimated to be $\gtrsim 0.2 \text{ Jy}$ at the redshifted 21-cm frequency.³ This gave eleven sources which we observed (Table 1), eight of which were not completely ruined by RFI, and as seen from Fig. 1, all are believed to be below the critical luminosity. For the $\approx 40\%$ detection rate at $L_{1216} \lesssim 10^{23} \text{ W Hz}^{-1}$, we therefore expect approximately three detections, although there were none. We discuss possible reasons for the exclusive non-detections in this paper.

2 OBSERVATIONS AND DATA REDUCTION

2.1 Green Bank observations

Each of the sources targetted with the Green Bank Telescope were observed for a total of two hours on source, with the aim of reaching an r.m.s. noise level of $\lesssim 5 \text{ mJy per } 10 \text{ km s}^{-1} \text{ channel}$ (for $T_{\text{sys}} = 70 \text{ K}$). This gives a 3σ optical depth limit of $\tau \approx 0.03$ per channel for a flux density of 0.5 Jy , i.e. a sensitivity to $N_{\text{HI}} \approx 3 \times 10^{17} (T_{\text{spin}}/f) \text{ cm}^{-2}$, the lower limit for most of the published searches (see figure 4 of Curran et al. 2008). We used the RCVR.342 receiver backed with the GBT Spectrometer in narrow bandwidth, high resolution mode in $4 \times 12.5 \text{ MHz}$ bands, while maintaining a redshift coverage of $\Delta z \approx \pm 0.06$ in each band. Each source was observed in two orthogonal linear polarisations which, after flagging of bad data, were averaged together (using the GBTIDL software):

NVSS J012142+132058 was observed at 314.53 MHz on 17 June 2010, over 4096 channels, giving a spacing of 3.052 kHz (2.92

km s^{-1}). After flagging of the worst RFI affected scans, 0.6 hours of data remained with an average system temperature of $T_{\text{sys}} = 90 \text{ K}$, although some spikes were still present in the bandpass (Fig. 2). **NVSS J020510+224250** was observed at 315.23 MHz on 31 August 2010, over 4096 channels, giving a spacing of 3.052 kHz (2.91 km s^{-1}). $T_{\text{sys}} = 87 \text{ K}$ and the YY polarisation exhibited negative fluxes for the whole observations and after flagging out the worst RFI affected on the XX polarisation 0.68 hours of data remained.

NVSS J023111+360027 was observed at 348.22 MHz on 1 September 2010, over 8196 channels, giving a spacing of 1.526 kHz (1.31 km s^{-1}). After flagging, 0.74 hours of data remained, although all of the scans exhibited negative fluxes. $T_{\text{sys}} = 75 \text{ K}$ and between the RFI spikes, the r.m.s. noise levels were low (4 mJy per 10 km s^{-1}), although the spikes raised the mean to 189 mJy over the observed range.

WN J0617+5012 was observed at 342.02 MHz on 6 July 2010, over 8196 channels, giving a spacing of 1.526 kHz (1.34 km s^{-1}). The mean system temperature was 76 K and after flagging, 0.63 hours of data remained. There is an “absorption feature” close to the expected redshift of $z = 3.153$ (fitted by two narrow Gaussians at an offset of 220 and 241 km s^{-1} from 0 km s^{-1} , defined by 342.02 MHz), which is present on all four sub-averages of the data. However, this is also true for the two “emission features” at ≈ -1500 and -1100 km s^{-1} and so we must attribute these to RFI. Again, the regions between the spikes had low r.m.s. noise levels (5 mJy per 10 km s^{-1}), although in Table 1 we quote the value over 337.56–343.17 MHz, where the spikes are fairly weak.

PKS 0742+10 was observed at 390.30 MHz on 13 August 2010, over 16384 channels, giving a spacing of 763 kHz (0.59 km s^{-1}). After flagging of the worst RFI affected scans, 0.6 hours of data remained with an average system temperature of $T_{\text{sys}} = 81 \text{ K}$. However, intermittent spikes remained, meaning that the r.m.s. noise level quoted in Table 1 only applies to the clean regions between these, with a spike being present over $z = 2.6302 - 2.6309$ (391.20–391.27 MHz), very close to the emission redshift of the source.

FIRST J074729.3+365438 was observed at 355.81 MHz on 7 June 2010, over 16384 channels, giving a spacing of 763 kHz (0.66 km s^{-1}). The mean system temperature was 63 K and 0.8 hours of data remained after flagging the integrations affected most by RFI. As seen in Fig. 2, the bandpass was still dominated by spikes and so in Table 1 we quote the r.m.s. noise level over the relatively clear 355.78–357.15 MHz.

NVSS J092022–071217 was observed at 377.77 MHz on 9 September and 29 December 2010, over 16384 channels, giving a spacing of 763 kHz (0.61 km s^{-1}). The mean system temperature was 65 K and flagging of badly affected data gave a total integration time of 0.63 hours. Even so, the bandpass was still dominated by spikes with RFI close to the expected frequency of the redshifted 21-cm line preventing us from assigning a limit.

B2 1121+31B was observed at 336.83 MHz in three sessions spanning from 6 July to 5 August 2010. The band was split over 4096 channels, giving a spacing of 3.052 kHz (2.73 km s^{-1}). The mean system temperature was 62 K and RFI was minimal, with 0.90 hours of data remaining after flagging the worst of this. Despite the absence of severe RFI and the flat bandpasses, like J0205+2242 each scan exhibited a negative flux, in both polarisations, over the whole run. Negative fluxes can often caused by a region of high confusion leading to the off-measurement being stronger than the source. At 337 MHz, the half-power beam width of the GBT is $\sim 40'$, within which the NASA/IPAC Extragalactic Database lists 17 000 sources, 140 of which are classified as radio sources. There-

² Applying the $B - z$ curve (figure 5 of Curran et al. 2009), gives $B \gtrsim 22$ for $L_{1216} \lesssim 10^{23} \text{ W Hz}^{-1}$ at these redshifts.

³ Except for J0617+5012 for which no fluxes were available from the NASA/IPAC Extragalactic Database, although we report 1.28 Jy at 342 MHz here.

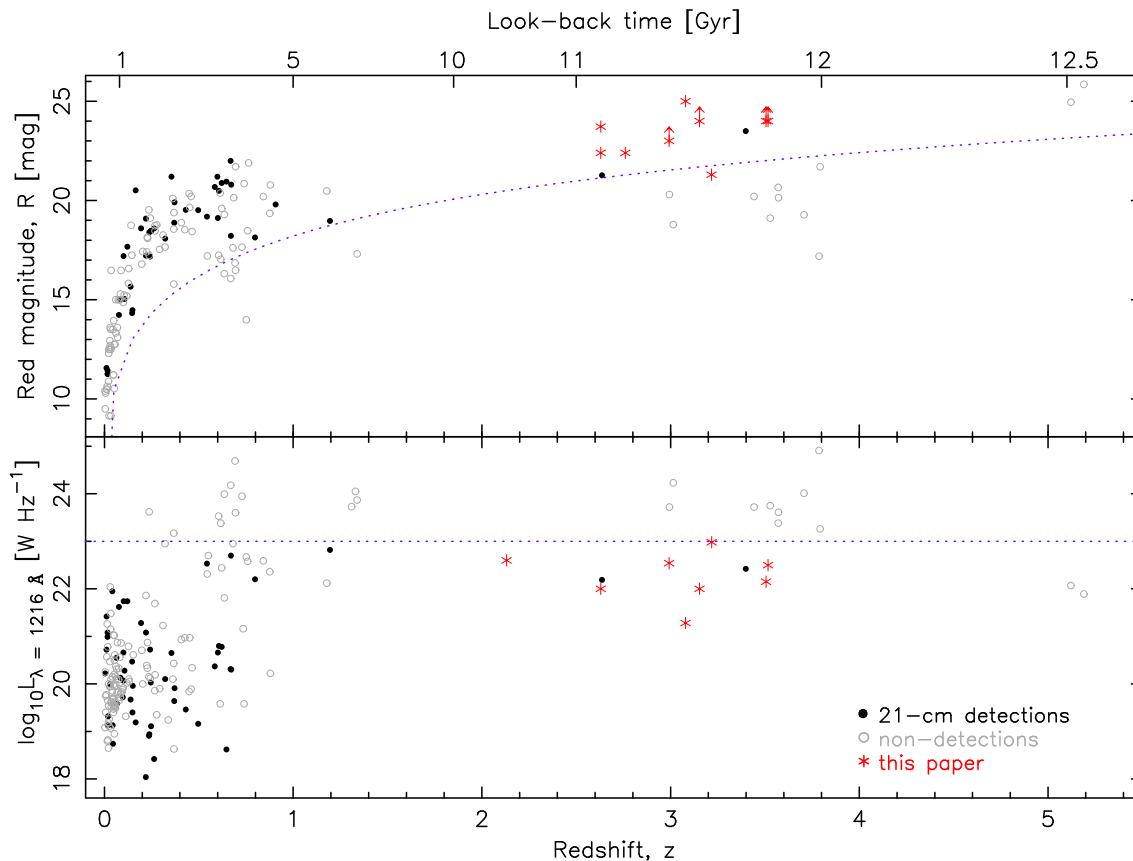


Figure 1. The red magnitude (top) and $\lambda = 1216 \text{ \AA}$ continuum luminosity (bottom) for the redshifted associated 21-cm searches (compiled in Curran & Whiting 2010; Allison et al. 2012). The filled symbols show the detections and the unfilled symbols the non-detections, with the asterisks showing our targets (all of which are non-detections), i.e. the eleven points in the top panel and the eight for which useful data were obtained in the bottom panel (with L_{1216} as originally estimated and not corrected for extinction, as the remaining points are). In the top panel the curve shows which B magnitude corresponds to $L_{1216} = 10^{23} \text{ W Hz}^{-1}$ for a spectral slope of $\alpha = -1.5$ (cf. figure 5 of Curran et al. 2009) used to select the targets and in the bottom panel the line signifies $L_{1216} = 10^{23} \text{ W Hz}^{-1}$, above which associated 21-cm has never been detected. Note that for J0231+3600, at $z = 3.079$, $I = 25.0$ is shown (Table 1).

fore confusion within the beam/sidelobes/off-position leading to a negative flux is a possibility. Although the flux levels may be not be properly calibrated, the data themselves are believed to be reliable (Ries 2012), as is apparent from the consistency between scans for both J0205+2242 and 1121+31B.

2.2 Westerbork observations

For the WSRT observations we requested four hours for each source using all 15 antennas (giving 105 baseline pairs), with the aim of reaching an r.m.s. noise level of $\lesssim 20 \text{ mJy}$ per 10 km s^{-1} channel. For a flux density of 0.5 Jy , this gives a 3σ optical depth limit of $\tau \approx 0.1$ per channel, a sensitivity to $N_{\text{HI}} \gtrsim 2 \times 10^{18} (T_{\text{spin}}/f) \text{ cm}^{-2}$. We used the UHF-low receiver backed with the correlator over $2 \times 5 \text{ MHz}$ bands, each in two polarisations over 1024 channels, in order to have a channel spacing of $\approx 4 \text{ km s}^{-1}$, while maintaining a redshift coverage of $\Delta z \approx \pm 0.04$. For each source the delays were all self calibrated with 3C 48, 3C 147 and 3C 286 being used for bandpass calibration and the data were reduced using the MIRIAD interferometry reduction package, with a spectrum being extracted from each cube. As per the GBT spectra, these are shown in Fig. 2 and summarised in Table 1:

NVSS J012142+132058 was observed on 5 January 2010 for a

total of 5.0 hours. Severe RFI meant that extensive flagging of the data was required, leaving 45 baseline pairs. Despite the flagging, a reasonable image could not be produced and so a spectrum was obtained by averaging together the remaining baseline pairs, giving a much reduced flux with two spikes remaining. An r.m.s. noise level of 10 mJy per 10 km s^{-1} channel was reached between these spikes, which rises to 134 mJy averaged over the whole bandpass. Each unsmoothed channel was 4.66 km s^{-1} wide and the synthesised beam was $772'' \times 83''$.

NVSS J020510+224250 was observed on 19 February 2010 for a total of 5.0 hours. Again severe RFI required extensive flagging, leaving only the XX polarisation and 78 baseline pairs which produced a poor quality image. A spectrum was, however, extracted from the cube, which had an r.m.s. noise level of 77 mJy per 10 km s^{-1} channel between the two main spikes, which rises to 130 mJy over the whole bandpass. Each unsmoothed channel was 4.64 km s^{-1} wide and the synthesised beam $237'' \times 61''$.

NVSS J023111+360027 was observed on 10 February 2010 for a total of 3.5 hours. Again, RFI required extensive flagging, leaving only 55 baseline pairs. From this an image of the target could not be produced, with patchy emission over the field being evident as a ripple in the extracted spectrum. Each unsmoothed channel was 4.20 km s^{-1} wide and the synthesised beam $256'' \times 69''$.

B20300+37A was observed for 2.7 hours on 14 December 2009

for 4.5 hours. After flagging 66 baselines remained, but RFI was still too severe to allow us to produce an image and so we show the average of the unflagged baseline pairs. Each unsmoothed channel was 3.61 km s^{-1} wide.

WN J0617+5012 was observed at 342.02 MHz for 6.0 hours on 18 January 2010, but severe RFI meant that no data could be used.

PKS 0742+10 was observed at 390.30 MHz for 5.8 hours on 14 December 2009, but again, severe RFI marred the whole observation.

FIRST J074729.3+365438 was observed at 355.81 MHz for 6.0 hours on 11 March 2010. After flagging the worst RFI, 55 baseline pairs remained from which an image of the target could not be produced. Nevertheless, the spectrum extracted from the field was relatively spike free and, as in the case of J0231+3600, there is a strong ripple evident, although the spectrum is very noisy. Each unsmoothed channel was 4.10 km s^{-1} wide and the synthesised beam was $244'' \times 66''$.

VLSS J1115.1+5016 was observed at 401.24 MHz on 12 December 2009 for 4.0 hours. However, severe RFI in this band meant that none of the data were useable.

B2 1121+31B was observed at 336.83 MHz for 5.2 hours on 19 January 2010. After flagging, 66 baseline pairs remained from which an image was produced. The image was of poor quality and the extracted spectrum is over the central $\pm \approx 15'$, with the flux density showing a strong dependence on the extent of the image used, thus limiting the reliability of this. Each unsmoothed channel was 4.35 km s^{-1} wide and the synthesised beam was $288'' \times 62''$.

B2 1240+39 was observed at 453.66 MHz for 3.0 hours on 5 April 2010. After flagging, 55 baseline pairs remained and a spectrum was extracted from the cube. Each unsmoothed channel was 3.27 km s^{-1} wide and the synthesised beam was $303'' \times 73''$.

3 POSSIBLE REASONS FOR THE NON-DETECTION OF 21-CM

3.1 Sensitivity limits

Despite our deliberate selection of optically faint sources, with continuum luminosities below the threshold of $L_{1216} = 10^{23} \text{ W Hz}^{-1}$, we have not detected H I 21-cm in any of the eight sources for which there were useable data. Below this critical value, Curran & Whiting (2010) find a $\gtrsim 40\%$ general detection rate, which consists of $\approx 50\%$ for compact objects⁴ and $\approx 40\%$ for others. That is, we may expect approximately three detections out of the eight sources for which the data were not overwhelmed by RFI.

One possible reason for the non-detections is that all of the sources were affected to some degree by RFI, giving some relatively poor sensitivity limits (Table 1), where detections of optical depths of $\tau_{\text{obs}} \gtrsim 0.1$ have been documented to be in the minority (Vermeulen et al. 2003; Morganti 2004). In order to investigate this, in Fig. 3 we show the obs optical depths for all the redshifted 21-cm searches. Since many of our sources were observed by both

the GBT and WSRT, we use the best limit in each case and smooth these, as well as rebinning the 3σ limits from the literature, to a channel spacing of 167 km s^{-1} , the mean FWHM of the 21-cm detections. This normalises all of the limits, published at various spectral resolutions, and gives the limit for the detection of putative line of width $\text{FWHM} = 167 \text{ km s}^{-1}$ within a single channel.

This normalisation has the effect of moving all of our limits to $\tau_{\text{obs}} \lesssim 0.1$, while degrading the column density limits (see Fig. 5) by a factor of ≈ 4 to those quoted in Table 1. From Fig. 3, we see that our limits are located in the densest clustering of the detections and so for the rest of the analysis, since we are attempting to explain the exclusive non-detections, we assume that (at least some of) the targets have been searched sufficiently deeply.

We note also a weak correlation between the obs optical depth and the profile width (left panel)⁵, which may suggest that weak, wide profiles may be missed by 21-cm surveys, despite having similar column densities to the detections (Allison et al., in prep.). For completeness, we also show how the optical depth is distributed with redshift (middle panel) and the rest frame 1.4 GHz flux density, from which we see the expected anti-correlation.

3.2 Radio properties

A possible effect which could reduce the probability of detecting 21-cm absorption is the non-deliberate selection of these high redshift radio galaxies having steep radio spectra (all, apart from B0742+10 being ‘‘Ultra-Steep Spectrum Radio Sources’’, De Breuck et al. 2002). This may have an effect on the *actual* optical depth of the line, τ , which is related to the *observed* optical depth, $\tau_{\text{obs}} \equiv \Delta S/S$, through $\tau \equiv -\ln\left(1 - \frac{\Delta S}{Sf}\right)$, where f , the covering factor, quantifies how much of the observed flux is intercepted by the absorber. In the optically thin regime (where $\Delta S \lesssim 0.3 S$), this expression reduces to $\tau \approx \Delta S/(Sf) = \tau_{\text{obs}}/f$. Since, by definition, $f \leq 1$ then the actual optical depth limit is $\tau \geq \tau_{\text{obs}}$.⁶ That is, the limit is affected by how effectively the absorbing gas intercepts the background emission.

Unfortunately, for this sample there is only high resolution radio imaging available for one source – B0742+10, which subtends 1.2 mas at 15 GHz (Stanghellini et al. 2001). At $z = 2.630$ this corresponds to a linear extent of 10 pc (using a standard Λ cosmology with $H_0 = 71 \text{ km s}^{-1} \text{ Mpc}^{-1}$, $\Omega_{\text{matter}} = 0.27$ and $\Omega_{\Lambda} = 0.73$). Of the remainder of the sample, only four are in the area of sky currently covered by the Very Large Array’s FIRST (Faint Images of the Radio Sky at Twenty Centimetres) survey, having deconvolved minor axes of $0.91''$ (7 kpc) for J0747+3654, $1.02''$ (8 kpc) for J0920–0712, $1.58''$ (12 kpc) for B1121+31B and $0.75''$ (6 kpc) for B1240+39. Since these are typically unresolved by the $5''$ synthesised beam, assigning a source size of $\lesssim 40 \text{ kpc}$ for each component may be more apt. For J0121+1320, J0205+2242, J0231+3600, B0300+37A and J0617+5012, which are all unresolved by the NRAO VLA Sky Survey (NVSS), the typical $17''$ minor axis of the beam gives source sizes of $\lesssim 130 \text{ kpc}$ for these redshifts.

Given the lack of high resolution radio imaging, information

⁴ Gigahertz peaked spectrum (GPS), compact steep spectrum sources (CSS) and compact symmetric objects (CSO). Although the 21-cm detection rate is generally believed to be higher for these than the general population, when the $L_{1216} \geq 10^{23} \text{ W Hz}^{-1}$ sources are removed the rates are similar, indicating that the higher rates may be due to the generally low ultra-violet luminosities of the compact objects (Curran & Whiting 2010).

⁵ The observed distribution has a 1.4% probability of occurring by chance, which is significant at 2.46σ , assuming Gaussian statistics.

⁶ Since f is generally unknown (see Curran 2012), we leave this (as well as the spin temperature) as a free parameter (Table 1). Assuming f has its maximum value of unity, as if often the case in the literature, improves the perceived sensitivity of the observation, where in fact $f < 1$.

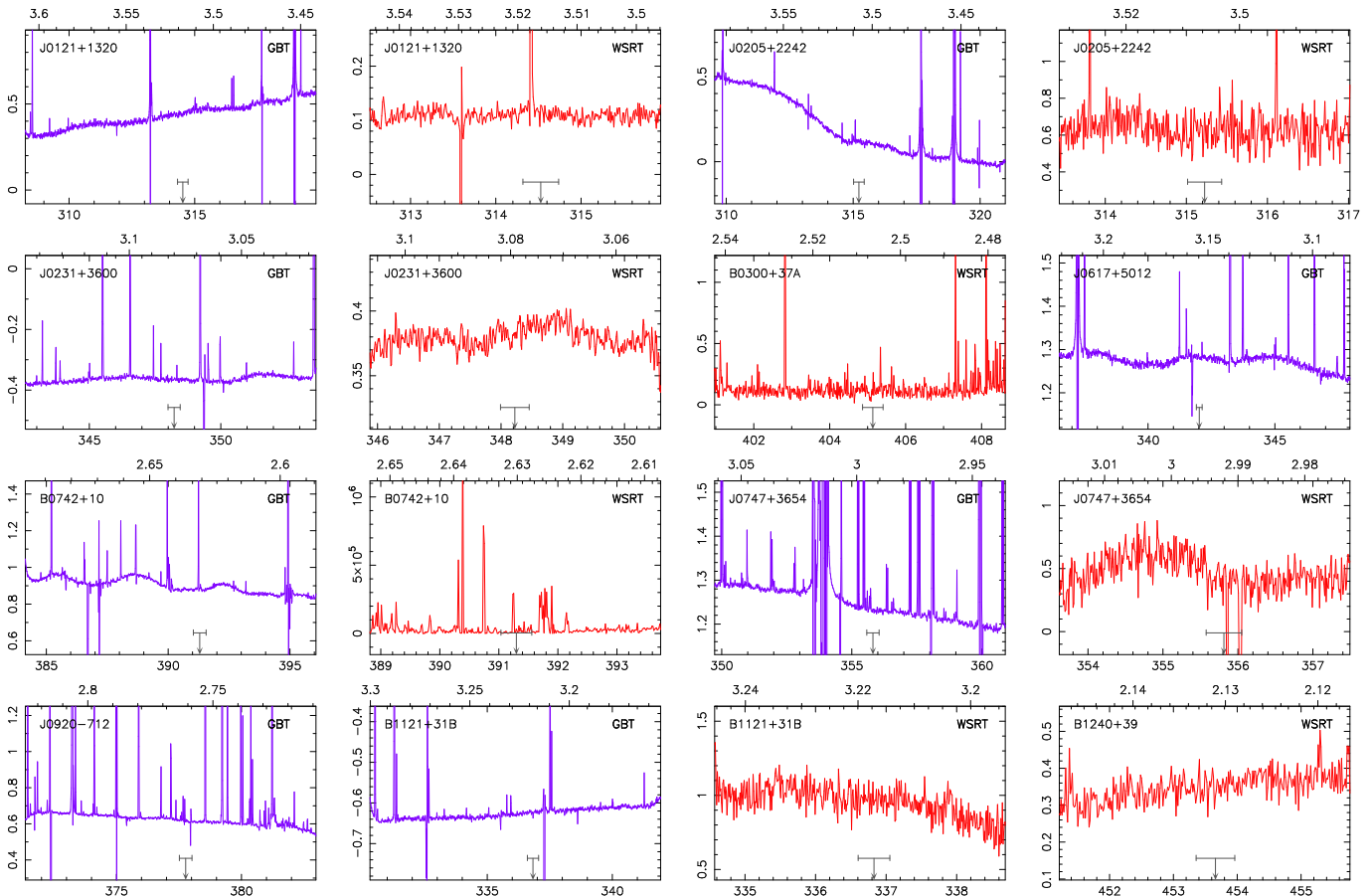


Figure 2. The spectra from the H I 21-cm searches shown at a spectral resolution of 10 km s^{-1} . The ordinate gives the flux density [Jy] and the abscissa the barycentric frequency [MHz]. The downwards arrow shows the expected frequency of the absorption from the optical redshift, with the horizontal bar showing a span of $\pm 200 \text{ km s}^{-1}$ for guidance. The scale along the top axis shows the redshift of H I 21-cm.

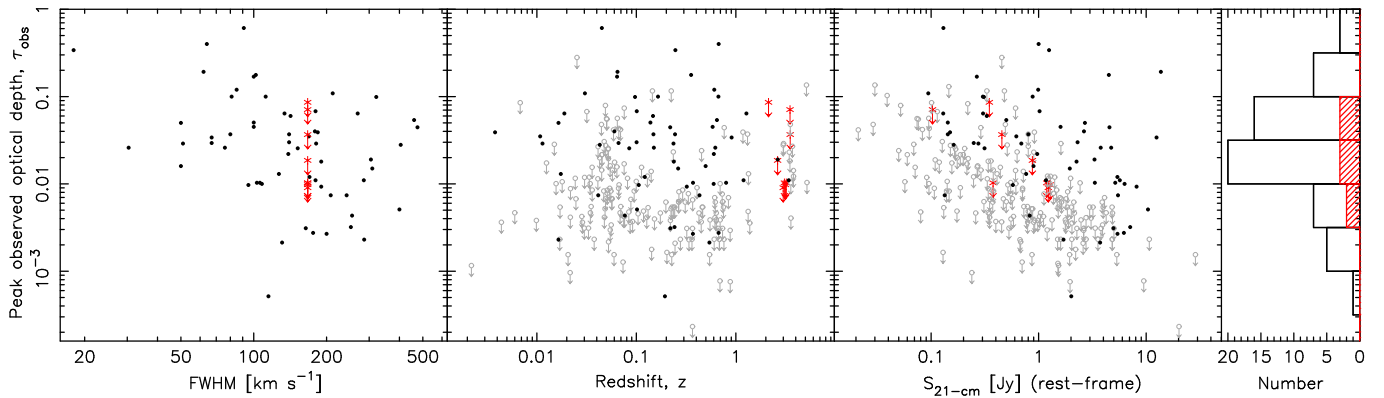


Figure 3. The observed optical depth versus the FWHM of the profile (left), redshift (middle) and rest-frame 1.4 GHz flux density (right). The symbols are as per Fig. 1, where in the left panel, for the sake of clarity, only our limits are shown. These, and the other limits in the remaining panels, have been resampled to a spectral resolution of 167 km s^{-1} , the mean of the detections which range from 18 to 475 km s^{-1} (Carilli et al. 1992 and Vermeulen et al. 2003, respectively). The unfilled histogram shows the distribution for the detections and the hatched histogram the limits to our eight targets not overwhelmed by RFI.

on the source size may be gleaned from the radio SEDs, given that the turnover frequency is anti-correlated with the size of the radio source (Fanti et al. 1990). In order to explore this possibility, in Fig. 4, we show the spectral energy distributions (SEDs) of our eight targets, from which the derived turnover frequencies and spectral indices are summarised in Table 2. From this

we see that B0742+10 is the only source with an indisputable turnover, consistent with its observed compactness (10 pc at 15 GHz, Stanghellini et al. 2001). Given that none of the other sources exhibit a *clear* turnover above the lowest frequency which has been

Table 1. The observational results for the $\gtrsim 0.2$ Jy optically faint northern sources which fall into the GBT and WSRT 90-cm bands. With the exception of B0742+10 (which is from Wall & Peacock 1985), all are ultra-steep spectrum sources (from De Breuck et al. 2002). The second and third columns list the magnitudes and their values. The fourth column gives the source redshift, followed by the observed frequency range [MHz] over which ΔS , the r.m.s. noise [mJy] reached per 10 km s^{-1} channel, is applicable. S is the continuum flux density [Jy] and $\tau_{\text{obs}} = -\ln(1 - 3\Delta S/S_{\text{cont}})$ gives the 3σ limit to the observed optical depth of the line per 10 km s^{-1} channel. This is followed by the resulting neutral hydrogen column density, where $N_{\text{HI}} = 1.823 \times 10^{18} (T_{\text{spin}}/f) \int \tau_{\text{obs}} dv [\text{cm}^{-2} \text{ K}^{-1}]$, T_{spin} being the spin temperature and f the covering factor (see Sect. 3.2). Lastly we list the redshift range over which the limit applies.

Source	Mag	Value	z	ν_{obs}	ΔS	S	τ_{obs}	Tel.	$N_{\text{HI}} \cdot (f/T_{\text{spin}})$	z-range
0121+1320	r_S	> 24	3.516	313.43–316.40	23	0.455	< 0.15	GBT	$< 2.7 \times 10^{18}$	3.4893–3.5318
...	312.11–317.06	10	0.103	< 0.29	WSRT	$< 5.3 \times 10^{18}$	3.4799–3.5510
J0205+2242	r_S	> 24	3.506	309.93–317.60	24	0.251	< 0.29	GBT	$< 5.3 \times 10^{18}$	3.4723–3.5830
...	367.57–372.16	77	0.574	< 0.51	WSRT	$< 9.3 \times 10^{18}$	2.8167–2.8643
J0231+3600	I	25.0	3.079	342.68–353.46	189	—	—	GBT	—	—
...	345.80–350.75	5.3	0.377	< 0.042	WSRT	$< 7.7 \times 10^{17}$	3.0496–3.1076
B0300+37A	r_S	23.2	2.506	400.94–408.65	—	—	—	WSRT	—	—
J0617+5012	R	> 24	3.153	337.56–343.17	17	1.277	< 0.040	GBT	$< 7.3 \times 10^{17}$	3.1391–3.2079
...	339.59–344.53	—	—	—	WSRT	—	—
B0742+10	R	23.7	2.630	391.32–394.74	22	0.874	< 0.076	GBT	$< 1.4 \times 10^{18}$	2.5983–2.6298
...	388.78–393.61	—	—	—	WSRT	—	—
J0747+3654	r_S	> 23	2.992	355.78–357.15	15	1.232	< 0.037	GBT	$< 6.7 \times 10^{17}$	2.9771–2.9923
...	353.39–358.34	100	0.466	< 1.0	WSRT	$< 1.8 \times 10^{19}$	2.9638–3.0194
J0920–0712	R	22.4	2.760	—	—	0.621	—	GBT	—	—
J1115+5016	r_S	> 24	2.540	396.21–406.21	—	—	—	WSRT	—	—
B1121+31B	r_S	21.3	3.217	332.74–337.16	7.9	—	< 0.042*	GBT	$< 7.7 \times 10^{17}$	3.2129–3.2688
...	334.56–338.70	66	0.876	< 0.23	WSRT	$< 4.2 \times 10^{18}$	3.1937–3.2456
B1240+39	r_S	23.6	2.131	451.17–456.15	39	0.348	< 0.41	WSRT	$< 7.5 \times 10^{18}$	2.1139–2.1483

Notes: *Derived by interpolating $S_{151 \text{ MHz}} = 1.19 \text{ Jy}$ (Waldram et al. 1996) and $S_{365 \text{ MHz}} = 0.525 \text{ Jy}$ (Douglas et al. 1996), giving a continuum flux of $S_{378 \text{ MHz}} \approx 0.57 \text{ Jy}$.

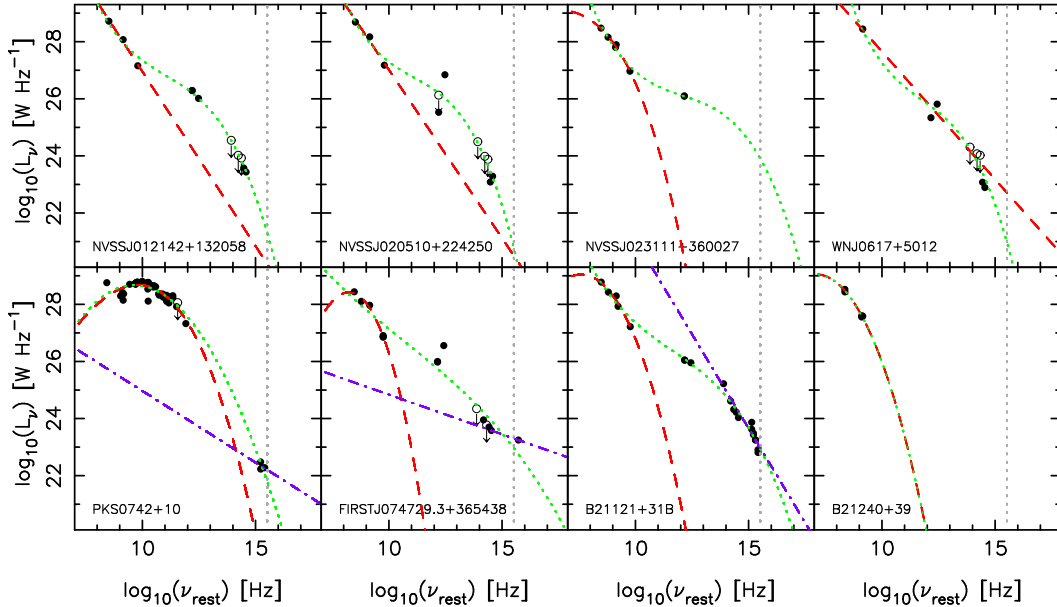


Figure 4. The SEDs of our eight targets not overwhelmed by RFI. The broken curve shows the fit to the radio data, the dotted line to the full data and the broken/dotted to the UV data, where possible (see the Appendix). The vertical dotted line signifies a rest-frame frequency of $3.29 \times 10^{15} \text{ Hz}$ ($\lambda = 912 \text{ \AA}$).

observed in the literature⁷, it is possible that the majority of our targets may have very extended radio morphologies, thus making $\tau \gg \tau_{\text{obs}}$ in the case of the limits.

In order to verify this through the comparison of the radio

SEDs with the rest of the 21-cm searched sources (compiled in Curran & Whiting 2010; Allison et al. 2012), we fit the radio SEDs (see the Appendix) and use the ASURV survival analysis package (Isobe et al. 1986) to obtain mean values of the turnover frequency and spectral index for various sub-samples (Table 3). From this it is seen that the mean turnover frequency for this sample is indeed lower than for any of the other sub-samples, indicating that the ra-

⁷ Whether there are turnovers in the SEDs of J0231+360, J0747+3654, B1121+31B and B1240+39 are disputable (Fig. 4).

Table 2. The radio properties and luminosities of the targets. ν_{TO} is the rest-frame turnover frequency [GHz], where the upper limits designate no observed turnover (which is thus assumed to occur below the observed frequencies), followed by the spectral index at the rest-frame 21-cm frequency, α . In the last three columns we list the $\lambda = 1216 \text{ \AA}$ (as originally estimated and not corrected for extinction) and $\lambda = 912 \text{ \AA}$ (as derived from the fits in the Appendix) rest-frame continuum luminosities [W Hz^{-1}], as well as the ionising ($\lambda \leq 912 \text{ \AA}$) photon rate [s^{-1}] in logs.

Source	ν_{TO}	α	L_{1216}	L_{912}	rate
J0121+1320	< 0.331	-1.22	22.50	—	—
J0205+2242	< 0.331	-1.18	22.15	—	—
J0231+360	< 0.302	-1.18	21.28	—	—
J0617+5012	< 1.41	-0.89	22.00	—	—
B0742+10	6.46	0.29	22.00	22.20	55.68
J0747+3654	0.17	-1.23	22.54	23.30	57.04
B1121+31B	0.040	-1.21	22.98	22.97	56.03
B1240+39	0.012	-1.50	22.60	—	—

Table 3. The mean values of the turnover frequency [Hz] and the spectral index at the rest-frame 1420 MHz for all of the sources searched in redshifted 21-cm absorption (Curran & Whiting 2010; Allison et al. 2012). n_p gives the number of data points and n_l the number of these which are limits. Note that the various sub-samples from the second row on exclude the current sources, which are summarised in the first row.

Sub-sample	TURNOVER FREQUENCY			SPECTRAL INDEX	
	$\langle \log_{10} \nu_{\text{TO}} \rangle$	n_p	n_l	$\langle \alpha \rangle$	n_p
This paper	7.91 ± 0.35	8	4	-1.02 ± 0.18	8
Detections	8.19 ± 0.14	56	23	-0.29 ± 0.08	58
Non-detections	8.03 ± 0.09	171	92	-0.39 ± 0.04	173
Dets + nons	8.07 ± 0.08	227	115	-0.37 ± 0.04	231
UV luminous	8.14 ± 0.29	19	11	-0.26 ± 0.12	19

radio sources are generally larger. However, this is based upon four limits to the turnover frequencies out of eight SEDs and, as warned by ASURV, may be unreliable.⁸ In the case of the spectral indices, where there are no limits, we see that the spectra of our sample are significantly steeper than for the other sub-samples.⁹ Thus, if the spectral index is a reliable tracer of the background source size, the fact that this sample consists almost exclusively of steep spectrum sources, indicating large radio source sizes, means that poor coverage of the background source cannot be ruled out as the cause of the non-detections. Note, however, for the “UV luminous” sources (the 19 which lie above the $L_{\text{UV}} = 10^{23} \text{ W Hz}^{-1}$ cut-off, Curran et al. 2011c), the mean spectral index is close to that of the 21-cm detections, thus ruling out the same predisposition towards large radio sources being the cause of the non-detections.

⁸ As seen from Fig. 4, it is conceivable that seven of the turnover frequencies are limits. Furthermore, the high redshift sources will also be subject to a higher mean turnover due to that fact that the lowest typical value, 74 MHz, is in the observed-frame, giving the high redshift sources higher upper limits in the rest-frame.

⁹ Note also that the non-detections have steeper indices than the detections, although these are consistent within the uncertainties.

3.3 Ionising luminosities and photon rates

Although all of our sources were selected to have $\lambda = 1216 \text{ \AA}$ continuum luminosities below the critical value of $L_{1216} \sim 10^{23} \text{ W Hz}^{-1}$ (Fig. 1), it is clear that the total ionising ($\lambda \leq 912 \text{ \AA}$) luminosity, $\int_{\nu_{\text{ion}}}^{\infty} (L_{\nu}/\nu) d\nu$, provides a much better measure of the ionising flux than a monochromatic value (be it L_{1216} or L_{912} , Curran & Whiting 2012). In equilibrium, the total ionising luminosity is related to the recombination of the atoms via (Osterbrock 1989),

$$\int_{\nu_{\text{ion}}}^{\infty} \frac{L_{\nu}}{h\nu} d\nu = 4\pi \int_0^{r_{\text{ion}}} n_p n_e \alpha_A r^2 dr, \quad (1)$$

where h is the Planck constant, giving the number of ionising photons per second. On the right hand side of the expression, n_p and n_e are the proton and electron densities, respectively, α_A the radiative recombination rate coefficient of hydrogen and r_{ion} is the extent of the ionisation (the “Strömgren sphere”). For a gas which decreases in density with increasing distance from the ionising source, Curran & Whiting (2012) show that $r_{\text{ion}} \rightarrow \infty$ for a finite ultra-violet luminosity and that for a large spiral this value is $L_{912} \sim L_{1216} \sim 10^{23} \text{ W Hz}^{-1}$, thus explaining this critical luminosity above which 21-cm absorption has never been detected.

From the mean SEDs of all of the associated 21-cm searches, the critical ionising photon rate arising from this luminosity is estimated to be $\int_{\nu_{\text{ion}}}^{\infty} (L_{\nu}/h\nu) d\nu = 2.9 \times 10^{56} \text{ s}^{-1}$ (Curran & Whiting 2012). From the polynomial fits (see the Appendix), we could determine photon rates for three of the targets presented here (Fig. 4), one of which is above the estimate of the critical value ($\log_{10}[2.9 \times 10^{56}] = 56.5$, cf. Table 2). Applying fits to each of the SEDs, the highest photon rate which could be determined for a 21-cm detection is $5.1 \times 10^{55} \text{ s}^{-1}$, which is below or close to the photon rate of the three targets ($\log_{10}[5.1 \times 10^{55}] = 55.7$, see Fig. 5). However, given that we have no estimates of the photon rates for the remaining five sources, from the previous estimates of the $\lambda = 1216 \text{ \AA}$ continuum luminosities (Table 2), it is possible that several of these have rates lower than for the three for which we do have estimates. For instance, J0121+1320 has been detected in CO emission (De Breuck et al. 2003), which may suggest a UV luminosity below the critical value, although further studies are required to find if this applies to the warm emitting molecular gas. While the monochromatic luminosities may not provide a reliable estimate of the photon rates, if, for the sake of argument, the remaining five sources do have ionising photon rates below the critical value, for a 40% detection rate (Sect. 3.1), the binomial probability of zero out of five detections is 0.078. This is significant at 1.76σ , assuming Gaussian statistics, and so not statistically important. Recalling that a possible reason for the non-detections is that the targets have not been searched sufficiently deeply (Sect. 3.1), this significance could be lower, thus not requiring us to “explain away” all eight non-detections.

Lastly, given that $\int_{\nu_{\text{ion}}}^{\infty} (L_{\nu}/h\nu) d\nu \approx 3 \times 10^{56} \text{ s}^{-1}$ is sufficient to ionise all of the gas in a large spiral, photon rates lower than this will completely ionise gas disks of correspondingly smaller scale-lengths (Curran & Whiting 2012). The sample presented here is at more than double the look-back time of the majority of 21-cm detections (Fig. 1) and so if there is any evolution in galactic morphology, with a larger fraction of smaller galaxies at higher redshift (Baker et al. 2000; Lanfranchi & Friaça 2003), we may expect the value of the critical photon rate to be lower at the redshifts searched here, making the detection of 21-cm absorption all the more difficult.

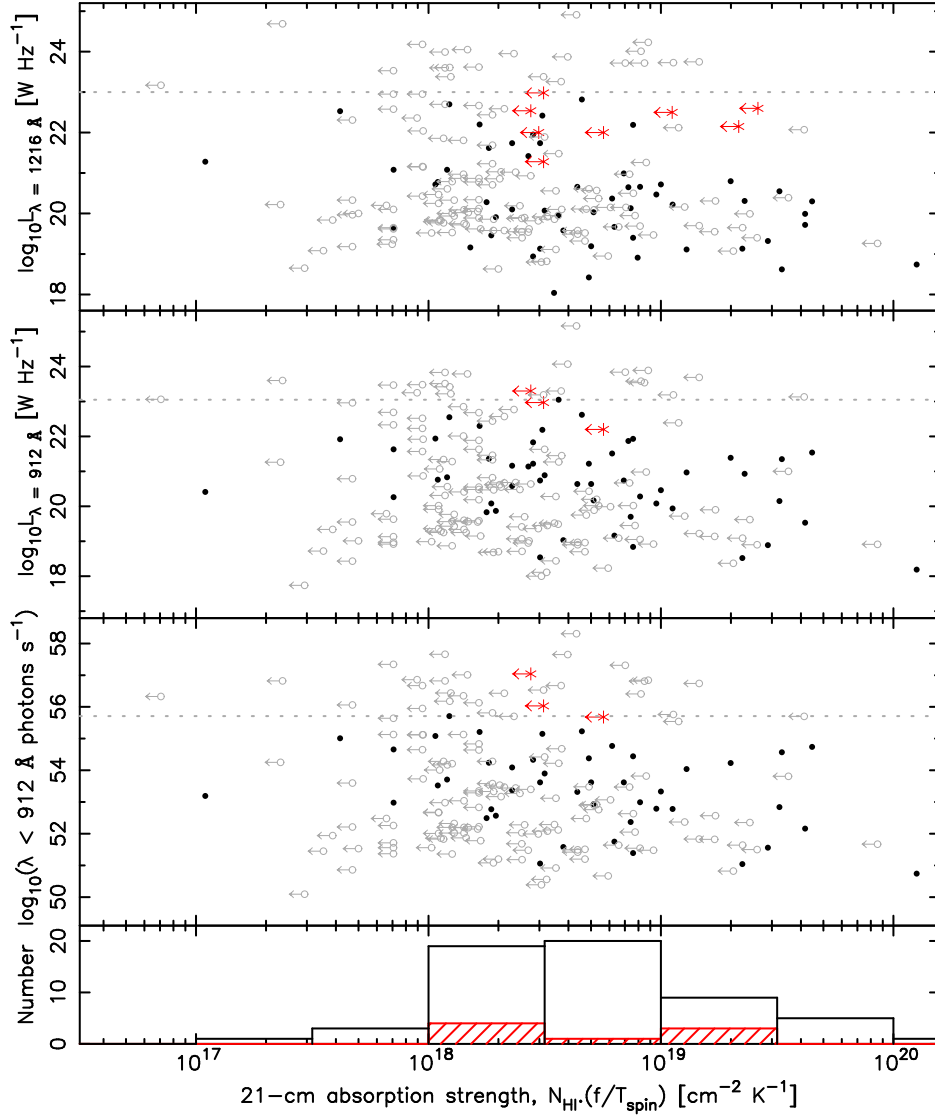


Figure 5. The $\lambda = 1216 \text{ \AA}$ continuum luminosity (top), $\lambda = 912 \text{ \AA}$ continuum luminosity (middle) and number of ionising photons per second (bottom) versus the 21-cm line strength ($1.823 \times 10^{18} \int \tau dv$), see Sect. 3.3. The horizontal lines in the top and middle panels show the critical monochromatic luminosity of $10^{23} \text{ W Hz}^{-1}$ and in the bottom panel $\int_{\nu_{\text{ion}}}^{\infty} (L_{\nu}/h\nu) d\nu = 5.1 \times 10^{55} \text{ s}^{-1}$, the highest photon rate at which a 21-cm detection occurs (see main text). The symbols are as per Fig. 1, with the left pointing arrows showing the 3σ upper limits to the 21-cm line strength (from Curran & Whiting 2010; Curran et al. 2011c; Allison et al. 2012). As per Fig. 3, these have been rebinned and integrated over a $\text{FWHM} = 167 \text{ km s}^{-1}$, which has the effect of degrading our limits by a factor of ≈ 4 in comparison to those quoted in Table 1 (see Curran 2012 for details). The unfilled histogram shows the distribution of the detection line strengths and the hatched histogram the limits to eight targets not overwhelmed by RFI.

Evolution may also play a rôle in that if the molecular (H_2) component constitutes a larger fraction of the gas at high redshift (Obreschkow & Rawlings 2009), lower relative column densities will make the H I more difficult to detect. However, as seen from Fig. 1, 21-cm has already been detected at $z \gtrsim 2$ and, although molecular gas has been detected in emission in over 100 ultra-luminous infrared galaxies (see Curran 2009; Curran et al. 2011a and references therein), searches for molecular absorption within the hosts of millimetre-loud sources have proved unfruitful (Curran et al. 2011b).¹⁰

¹⁰ Given that J0121+1320 is detected in CO emission and that a further five of the targets are known exhibit strong FIR emission (Fig. 4), these sources should be searched in the millimetre band to rule out the possibility of a

4 SUMMARY

We have undertaken a survey for the hydrogen apparently missing in high redshift radio galaxies and quasars by selecting targets in which the optical magnitudes indicate that these are below the UV luminosity cut-off, above which all of the gas is ionised (Curran & Whiting 2012). Despite this, there were no detections in the eight $z \gtrsim 2$ objects for which useful data were obtained. Upon

high molecular fraction suppressing the atomic abundance (if not already done so, although there are no published searches for molecular emission in the remaining targets). However, the cool absorbing molecular gas, rather than warm emitting component, may be expected to be coincident with the cool atomic gas (see Combes & Wiklind 1998; Murphy et al. 2001 and references therein).

an examination of the spectral energy distributions of the targets, we suggest two possible reasons for this:

(i) Due to our requirement of optically faint, radio-loud objects, for which their redshift placed them within the GBT and WSRT 90-cm bands, our sample was dominated by the ultra-steep spectrum sources of De Breuck et al. (2002). By fitting radio SEDs to these, we find a mean spectral index of $\langle\alpha\rangle = -1.0$, which is significantly higher than $\langle\alpha\rangle = -0.3$ and -0.4 for the 21-cm detections and the remaining non-detections, respectively. This suggests that most of our targets may have extended radio emission, thus reducing the coverage of the background flux by the absorbing gas, lowering the effective sensitivity of our survey.

(ii) Although our magnitude selection predicted that all of the targets are below the critical luminosity of $L_{UV} \sim 10^{23} \text{ W Hz}^{-1}$, those for which the ionising photon rate could be determined are above or close to 5.1×10^{55} ionising photons s^{-1} , the highest value which can be determined for a 21-cm detection. However, the photon rate could only be estimated for three of the eight sources and their monochromatic $\lambda = 1216 \text{ \AA}$ continuum luminosities may nevertheless suggest that these are below the threshold. Without sufficient blue/ultra-violet photometry, this is, however, speculation.

Although it is impossible at this time to determine which reason is main the culprit, note that the mean radio-band SEDs of the 19 sources for which $L_{1216} \gtrsim 10^{23} \text{ W Hz}^{-1}$, which initially highlighted a UV threshold, is no steeper than the SEDs of the 21-cm detections. This suggests that a bias towards larger radio sources is not the cause of the exclusive non-detections for the UV luminous sample. Also, presuming that the remaining five sources, for which the photon rate could not be determined, are below the threshold gives a detection rate (0 out of 5) which is not statistically significant, given the 40% chance of a detection at $z \lesssim 1$.

Furthermore, at these redshifts we are probing look-back times more than double that of the $z \lesssim 1$ sources and if there is a larger fraction of smaller galaxies at these epochs, the gas will be ionised at lower luminosities. For instance, the highest photon rate for which there exists a 21-cm detection ($5 \times 10^{55} \text{ s}^{-1}$), is sufficient to fully ionise a gas distribution of scale-length of 1.6 kpc (50% that of a large spiral, Kalberla & Kerp 2009), for $n_0 = 10 \text{ cm}^{-3}$ (Curran & Whiting 2012).¹¹ If this is the case, objects even fainter than those targeted here are required to find the missing hydrogen at high redshift, a task perhaps best suited for blind surveys with the Square Kilometre Array, where an optical redshift is not a prerequisite.

To conclude, although we cannot rule out the radio structure and other hitherto unforeseen high redshift effects as the source of the non-detections, the fact remains that $\lambda \leq 912 \text{ \AA}$ photons ionise hydrogen and there exists a 8.32×10^{-8} probability (a 5.36 σ significance) of the exclusive non-detections above a given ionising photon rate arising by chance (Curran & Whiting 2012). This is conjunction with the fact that the critical rate observed is just sufficient to ionise all of the gas in a large galaxy, leaves little doubt that photoionisation of the gas by the active nucleus is a dominant issue in the search of neutral gas within the hosts of these objects.

¹¹ For a disk, in which the thickness flares in the same manner as for the Milky Way (Kalberla et al. 2007), the total gas mass is estimated to be $M_{\text{gas}} = 1.3 \times 10^9 M_{\odot}$, a sixth of that found for a rate of 3×10^{56} ionising photons s^{-1} , the critical value estimated by Curran & Whiting (2012).

ACKNOWLEDGEMENTS

We wish to thank Gyula Józsa for coordinating all of the WSRT observations. This research has made use of the NASA/IPAC Extragalactic Database (NED) which is operated by the Jet Propulsion Laboratory, California Institute of Technology, under contract with the National Aeronautics and Space Administration. This research has also made use of NASA's Astrophysics Data System Bibliographic Services and ASURV Rev 1.2 (Lavalley et al. 1992), which implements the methods presented in Isobe et al. (1986). The Centre for All-sky Astrophysics is an Australian Research Council Centre of Excellence, funded by grant CE110001020.

REFERENCES

- Allison J. R., et al., 2012, MNRAS, 423, 2601
- Baker A. C., Mathlin G. P., Churches D. K., Edmunds M. G., 2000, in Favata F., Kaas A., Wilson A., eds, Star Formation from the Small to the Large Scale, Vol.45 of ESA SP ESA Special Publication, The Chemical Evolution of the Universe. Noordwijk, p. 21
- Carilli C. L., Perlman E. S., Stocke J. T., 1992, ApJ, 400, L13
- Combes F., Wiklind T., 1998, ESO Messenger, 91, 29
- Curran S. J., 2009, A&A, 497, 351
- Curran S. J., 2012, ApJ, 748, L18
- Curran S. J., Tanna A., Koch F. E., Berengut J. C., Webb J. K., Stark A. A., Flambaum V. V., 2011a, A&A
- Curran S. J., Webb J. K., 2006, MNRAS, 371, 356
- Curran S. J., Whiting M. T., 2010, ApJ, 712, 303
- Curran S. J., Whiting M. T., 2012, ApJ, in press (arXiv:1204.2881)
- Curran S. J., et al., 2011b, MNRAS, 416, 2143
- Curran S. J., et al., 2011c, MNRAS, 413, 1165
- Curran S. J., Whiting M. T., Webb J. K., 2009, Proceedings of Science, 89, Chap. 11
- Curran S. J., Whiting M. T., Webb J. K., Athreya A., 2011d, MNRAS, 414, L26
- Curran S. J., Whiting M. T., Wiklind T., Webb J. K., Murphy M. T., Purcell C. R., 2008, MNRAS, 391, 765
- De Breuck C., Neri R., Omont A., 2003, New Astronomy Review, 47, 285
- De Breuck C., van Breugel W., Stanford S. A., Röttgering H., Miley G., Stern D., 2002, AJ, 123, 637
- Douglas J. N., Bash F. N., Bozayan F. A., Torrence G. W., Wolfe C., 1996, AJ, 111, 1945
- Drinkwater M. J., Webster R. L., Francis P. J., Condon J. J., Ellison S. L., Jauncey D. L., Lovell J., Peterson B. A., Savage A., 1997, MNRAS, 284, 85
- Fanti R., Fanti C., Schilizzi R. T., Spencer R. E., Nan Rendong Parma P., van Breugel W. J. M., Venturi T., 1990, A&A, 231, 333
- Grasha K., Darling J., 2011, in American Astronomical Society Meeting Abstracts Vol. 43, A Search for Intrinsic HI 21-cm Absorption Toward Compact Radio Sources. p. 345.02
- Isobe T., Feigelson E., Nelson P., 1986, ApJ, 306, 490
- Kalberla P. M. W., Dedes L., Kerp J., Haud U., 2007, A&A, 469, 511
- Kalberla P. M. W., Kerp J., 2009, Ann. Rev. Astr. Ap., 47, 27
- Lanfranchi G. A., Friaça A. C. S., 2003, MNRAS, 343, 481
- Lavalley M. P., Isobe T., Feigelson E. D., 1992, in BAAS Vol. 24, ASURV, Pennsylvania State University. Report for the period Jan 1990 - Feb 1992.. pp 839–840

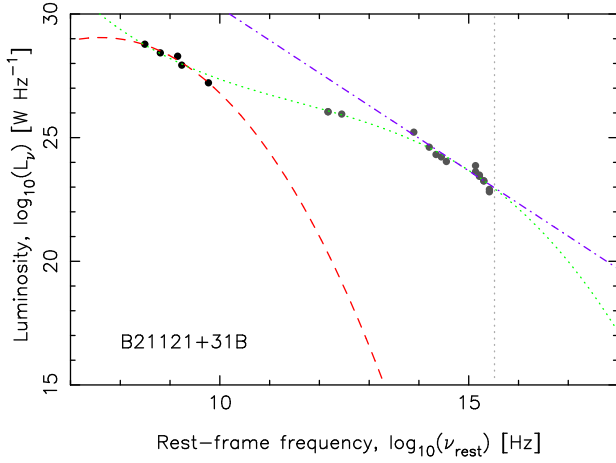


Figure 6. SED fits to B2 1121+31B. As coded in Fig. 4, the curves show the polynomial fits to the radio ($\nu_{\text{rest}} \leq 10^{12}$ Hz) data (dashed) and to the full ($\nu_{\text{rest}} \leq 10^{17}$ Hz) data (dotted). The straight dot-dashed line shows the power-law fit to the $10^{14.5} \leq \nu_{\text{rest}} \leq 10^{17}$ Hz data. The vertical dotted line highlights $\nu_{\text{rest}} = 3.29 \times 10^{15}$ Hz ($\lambda = 912$ Å).

- Morganti R., 2004, in Bachiller R., Colomer F., Desmurs J.-F., de Vicente P., eds, *European VLBI Network on New Developments in VLBI Science and Technology Probing the nature of the ISM in Active Galactic Nuclei through HI absorption*. pp 133–141
- Murphy M. T., Webb J. K., Flambaum V. V., Drinkwater M. J., Combes F., Wiklind T., 2001, *MNRAS*, 327, 1244
- Obreschkow D., Rawlings S., 2009, *ApJ*, 696, L129
- Osterbrock D. E., 1989, *Astrophysics of Gaseous Nebulae and Active Galactic Nuclei*. University Science Books, Mill Valley, California
- Press W. H., Flannery B. P., Teukolsky S. A., Vetterling W. T., 1989, *Numerical Recipes: The Art of Scientific Computing*. Cambridge University Press, Cambridge
- Ries P. A., 2012, PhD thesis, University of Virginia
- Schlegel D. J., Finkbeiner D. P., Davis M., 1998, *ApJ*, 500, 525
- Stanghellini C., Dallacasa D., O’Dea C. P., Baum S. A., Fanti R., Fanti C., 2001, *A&A*, 377, 377
- Vermeulen R. C., et al., 2003, *A&A*, 404, 861
- Waldram E. M., Yates J. A., Riley J. M., Warner P. J., 1996, *MNRAS*, 282, 779
- Wall J. V., Peacock J. A., 1985, *MNRAS*, 216, 173

APPENDIX — SED FITTING

In order to estimate the radio spectral indices and turnover frequencies, as well as the $\lambda \leq 912$ Å continuum luminosities and photon rates, we produced an SED for each source by compiling the NED photometries, the Galaxy Evolution Explorer (GALEX) near and far ultra-violet fluxes, as well as the *BVRK* magnitudes, published elsewhere (compiled in Curran et al. 2008; Curran & Whiting 2010). After correcting for Galactic extinction using the maps of Schlegel et al. (1998), for each of the 241 sources the flux density was converted to a luminosity and the frequency de-redshifted to the source rest-frame.

Using Vandermonde matrices (Press et al. 1989), three polynomials were fit to the data points for each source:

(i) *The radio SED:* A third or second order polynomial was fit to the $\nu_{\text{rest}} \leq 10^{12}$ Hz points. The turnover frequency was then

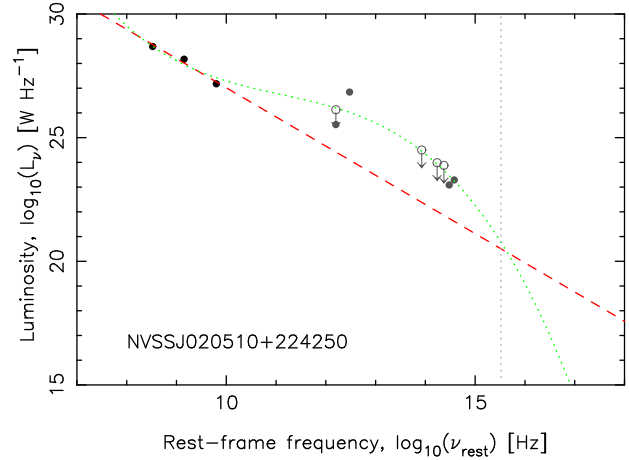


Figure 7. SED fits to NVSS J020510+224250 demonstrating a case where no radio turnover is apparent and where the $\lambda = 912$ Å continuum luminosity cannot be determined (cf. Fig. 6).

obtained from $dL_\nu/d\nu = 0$ (with a maximum being tested using $d^2L_\nu/d\nu^2 < 0$) and the spectral index from the value of $\alpha = dL_\nu/d\nu$ at $\nu_{\text{rest}} = 1.42 \times 10^9$ Hz, thus being defined as $S \propto \nu^\alpha$. Fig. 6 shows an example of a possible turnover (at 40 MHz) and a spectral index of $\alpha = -1.21$. In the case where no radio turnover is apparent, providing $dL_\nu/d\nu$ is negative in the radio-band, the lowest observed frequency is assigned as an upper limit to this (as in Fig. 7). That is, we assume that the turnover occurs at a frequency lower than that currently observed (Fanti et al. 1990). Otherwise, if $dL_\nu/d\nu \geq 0$, the source is flagged as having an indeterminate turnover frequency.

(ii) *The full SED:* A third order polynomial was fit to the all of the data points at $\nu_{\text{rest}} \leq 10^{17}$ Hz. This fit provides a visual guide only.

(iii) *The UV SED:* A first order polynomial (power-law) was fit to the $10^{14.5} \leq \nu_{\text{rest}} \leq 10^{17}$ Hz data. This upper cut-off is applied since, although relevant and used to derive the composite SEDs (Curran & Whiting 2012), the, usually sparsely sampled, X-ray points can have a strong influence on the fit, although these may be arising from other mechanisms than those producing the UV SED:

(a) Provided that $dL_\nu/d\nu < 0$ (e.g. as in Fig. 6), the UV SED was used to derive the luminosities and photon rate.

(b) Should the gradient exceed $dL_\nu/d\nu = 0$ at $\nu_{\text{rest}} = 3.29 \times 10^{15}$ Hz, usually from a concentration of data points, the luminosity is estimated from the mean of any neighbouring data points (at $\nu_{\text{rest}} = 10^{15.52 \pm 0.50}$ Hz).

Only in the first case (a), where a reliable fit is obtained over the range specified, is the ionising photon rate derived from

$$\int_{\nu}^{\infty} \frac{L_\nu}{h\nu} d\nu, \text{ where } \log_{10} L_\nu = \alpha \log_{10} \nu + C \Rightarrow L_\nu = 10^C \nu^\alpha$$

for a power-law fit, where α is the spectral index and C the intercept. This gives,

$$\frac{10^C}{h} \int_{\nu}^{\infty} \nu^{\alpha-1} d\nu = \frac{10^C}{\alpha h} [\nu^\alpha]_{\nu}^{\infty} = \frac{-10^C}{\alpha h} \nu^\alpha \text{ where } \alpha < 0,$$

otherwise the ionising photon rate is flagged as indeterminate.

Finally, in Fig. 8 we show the SED fits to the UV luminous sources (those which lie above the $L_{\text{UV}} = 10^{23}$ W Hz⁻¹ cut-off,

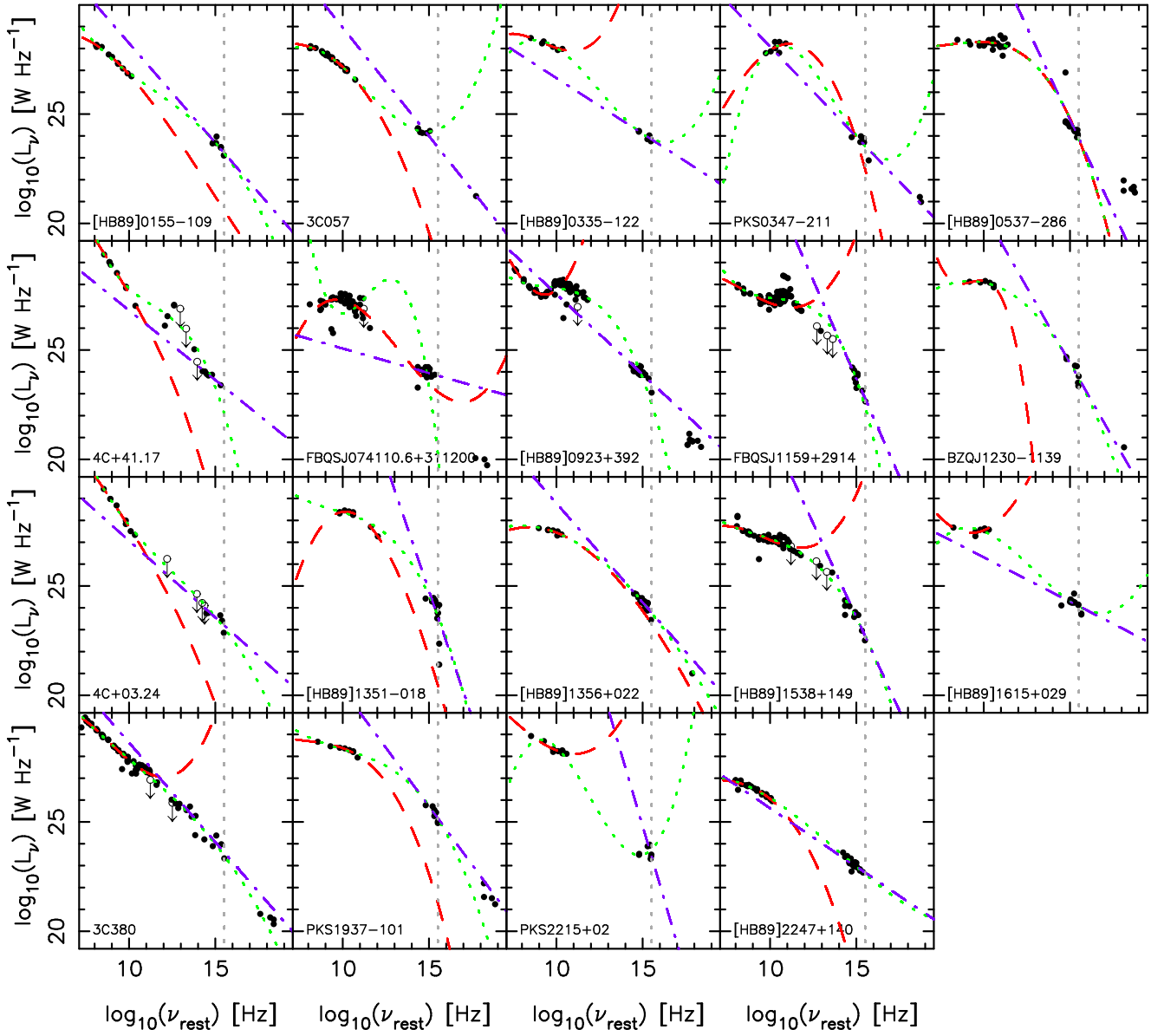


Figure 8. As per Fig. 4, but for the 19 UV luminous sources (Curran et al. 2011c).

the last row in Table 3). As seen from this, the ultra-violet luminosities may be estimated and photon rates derived for all of these (see Curran & Whiting 2012).